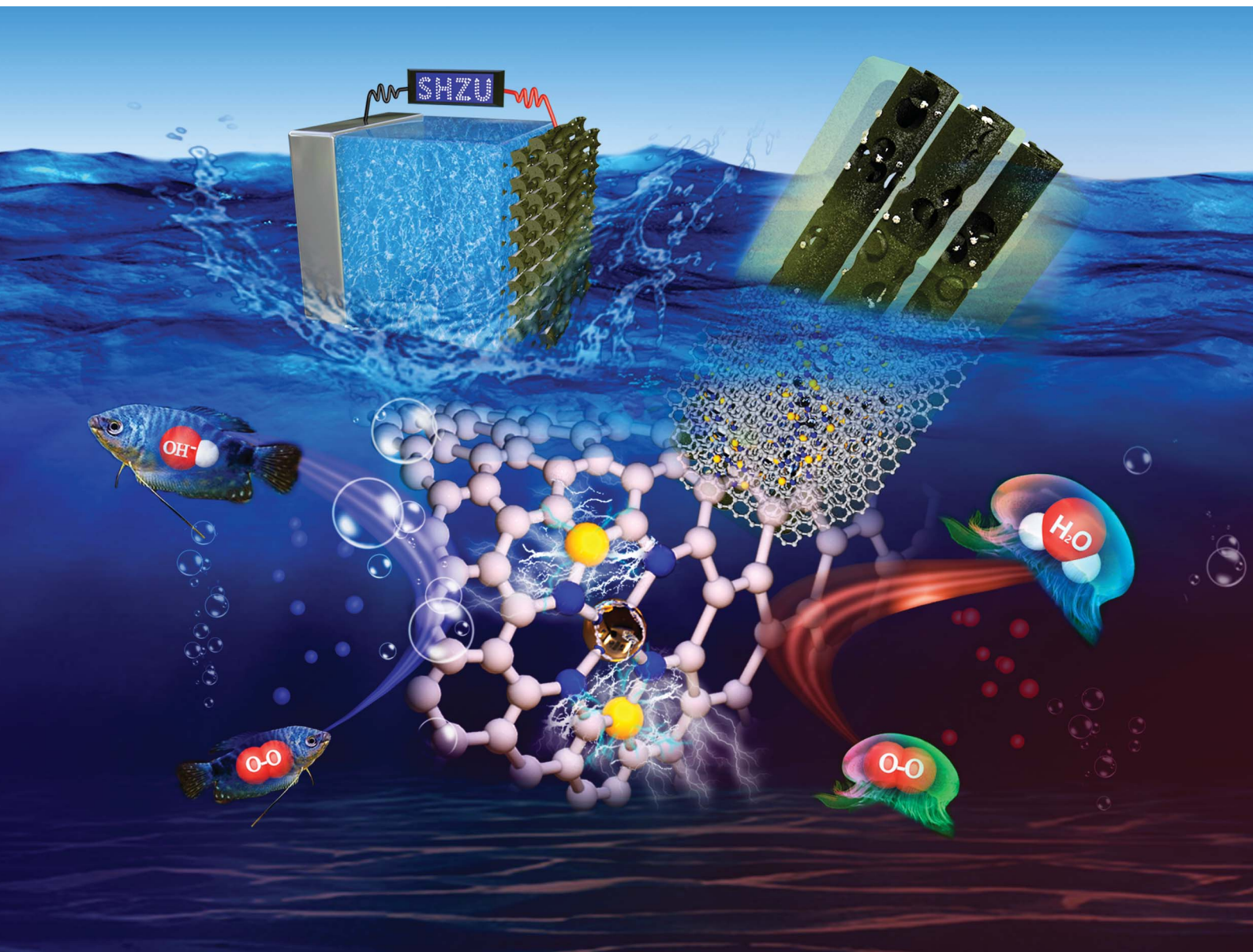


# Journal of Materials Chemistry A

Materials for energy and sustainability

rsc.li/materials-a



ISSN 2050-7488

**PAPER**

Xin Jia *et al.*

Isolated single iron atoms anchored on a N, S-codoped hierarchically ordered porous carbon framework for highly efficient oxygen reduction

Cite this: *J. Mater. Chem. A*, 2021, 9, 10110

# Isolated single iron atoms anchored on a N, S-codoped hierarchically ordered porous carbon framework for highly efficient oxygen reduction†

Xinghuan Liu,<sup>‡a</sup> Xingwu Zhai,<sup>‡a</sup> Wenbo Sheng,<sup>a</sup> Juan Tu,<sup>a</sup> Zeyu Zhao,<sup>a</sup> Yulin Shi,<sup>ID a</sup> Caixia Xu,<sup>ID a</sup> Guixian Ge<sup>ID b</sup> and Xin Jia<sup>ID \*a</sup>

Atomically dispersed metal catalysts are promising candidates for the oxygen reduction reaction (ORR) and for achieving efficient energy conversion. However, rational design of single atom catalysts (SACs) with high-efficiency ORR catalytic activity and superior stability is still crucial yet challenging. Herein, an *in situ* gas-foaming methodology is presented for constructing single Fe atoms dispersed on a N, S-codoped (Fe<sub>SA</sub>/NSC) hierarchically ordered porous carbon (HOPC) framework *via* one-step pyrolysis of dopamine (DA)/Fe<sup>3+</sup> complexes and thiourea in SBA-15 channels. HOPC structures (facilitating active site access and mass transfer) and optimized FeN<sub>4</sub>S<sub>2</sub> catalytic centers make Fe<sub>SA</sub>/NSC exhibit high ORR activity with a half-wave potential ( $E_{1/2}$ ) of 0.91 V, fuel selectivity and long-term stability (3 mV negative shift after 5000 potential cycles) in 0.1 M KOH. It even shows comparable ORR catalytic activity ( $E_{1/2} = 0.78$  V) to the Pt/C catalyst in acidic electrolytes. As the air electrode in zinc–air batteries, Fe<sub>SA</sub>/NSC demonstrates superior power density, long-term discharge stability and specific capacity to the commercial Pt/C catalyst. Thus, Fe<sub>SA</sub>/NSC is a promising non-platinum-group metal ORR catalyst for the ORR and application in zinc–air batteries.

Received 14th January 2021  
Accepted 24th March 2021

DOI: 10.1039/d1ta00384d

rsc.li/materials-a

## 1. Introduction

The oxygen reduction reaction (ORR) is a crucial process occurring in fuel cells, metal–air batteries and other energy conversion and storage devices.<sup>1–4</sup> However, the high thermodynamic potential energy and slow dynamics of four electron and proton transfer steps in the ORR limit its widespread applications.<sup>5,6</sup> Traditionally, platinum-group noble metals are believed to have prominent electrocatalytic activities for the ORR process, but the high cost, low abundance and poor stability limit their commercial applications.<sup>7,8</sup> In this regard, development of highly active, cost-effective and non-platinum metal catalysts for the ORR is of great significance for large scale applications.<sup>9,10</sup>

Single atom catalysts (SACs), especially non-platinum metal and nitrogen codoped carbon matrices (M = Fe, Co, Ni, Cu, Zn, Mn), would realize the utmost utilization of metal sites and

significantly benefit the ORR activity and stability.<sup>11–15</sup> Among these catalysts, Fe-based SACs have been widely considered as a promising candidate to replace Pt-based ORR catalysts.<sup>16–20</sup> However, Fe-based electrocatalysts still suffer from poor electrochemical stability and undesirable catalytic activity in acidic electrolytes.<sup>1,21,22</sup> Current reported strategies involve improving the metal loading,<sup>23,24</sup> doping heteroatoms<sup>25</sup> and designing dual-metal sites.<sup>26,27</sup> However, the most reported Fe content in Fe-based SACs is below 1.0 wt%, and a large amount of active Fe species are encapsulated in the carbon framework, which cannot participate in the reaction process of the ORR due to the inaccessibility of SACs.<sup>24,28</sup> Therefore, rational fabrication of Fe based SACs with superior ORR catalytic activity and stability is crucial yet challenging.

To cope with this challenge, optimizing the pore structures for the construction of SACs with large surface areas and outstanding conductivity would facilitate mass/electron transfer and significantly enhance the ORR activity.<sup>29,30</sup> Ordered mesoporous carbon (OMC) architectures,<sup>31</sup> a family of porous materials, have attracted widespread attention due to their large specific surface areas, excellent conductivity and strong resistance to corrosion.<sup>32</sup> However, OMC structures only have a single pore sized distribution, and a large number of active sites in the interior of OMC cannot participate in the ORR process. In addition, doping of metal/N with heteroatoms has been discovered to significantly influence the electronic structure center of the SACs and further boost the ORR

<sup>a</sup>School of Chemistry and Chemical Engineering, Key Laboratory for Green Processing of Chemical Engineering of Xinjiang Bingtuan, Key Laboratory of Materials-Oriented Chemical Engineering of Xinjiang Uygur Autonomous Region, Engineering Research Center of Materials-Oriented Chemical Engineering of Xinjiang Bingtuan, Shihezi University, Shihezi 832003, China. E-mail: jiaxin@shzu.edu.cn

<sup>b</sup>Key Laboratory of Ecophysics and Department of Physics, College of Science, Shihezi University, Shihezi, 832003, P. R. China. E-mail: geguixian@126.com

† Electronic supplementary information (ESI) available. See DOI: 10.1039/d1ta00384d

‡ These authors contributed equally to this work.

performance.<sup>33–35</sup> Thus, the design and synthesis of single atoms anchored on OMC with hierarchical structures and optimizing the coordination environment of SACs are efficient ways to enhance ORR catalytic activity in both acidic and alkaline media.<sup>36,37</sup>

Herein, inspired by our previous research, direct calcination of dopamine confined by graphitic carbon nitride ( $g\text{-C}_3\text{N}_4$ ) can form 2D N-doped graphene-like nanosheets.<sup>38</sup> We report a robust *in situ* gas-foaming approach for construction of accessible iron SACs on a hierarchically ordered porous N, S-codoped catalyst ( $\text{Fe}_{\text{SA}}/\text{NSC}$ ) for boosting the ORR activity *via* one-step pyrolysis of a dopamine (DA)/ $\text{Fe}^{3+}$  complex and thiourea in SBA-15 channels (Fig. 1a). The introduction of thiourea can provide nitrogen and sulfur source for anchoring more iron atoms and tuning the coordination environment of SACs. More importantly, thiourea plays the role of a sacrificial template for constructing HOPC structures in the process of carbonization. Such HOPC structures are especially essential in the ORR process owing to the following notable advantages: (1) numerous mesopore or micropore openings on the outer surfaces can significantly benefit movement of the electrolyte,

$\text{O}_2$  and reaction intermediates into or/and out of the channels; (2) the large BET specific surface areas and interpenetrating mesopore architecture can provide more active sites for the ORR and tremendously enhance the transport efficiency.<sup>39</sup> HOPC structures (facilitating active site access and mass transfer) and optimized  $\text{FeN}_4\text{S}_2$  catalytic centers (modifying the electronic structures of Fe– $\text{N}_4$  active centers) make  $\text{Fe}_{\text{SA}}/\text{NSC}$  exhibit superb oxygen reduction activity, stability and methanol tolerance in both acidic and alkaline media. In addition,  $\text{Fe}_{\text{SA}}/\text{NSC}$  also exhibits potential prospects in Zn–air batteries.

## 2. Experimental section

### 2.1 Materials

Dopamine (DA) hydrochloride and Nafion (5 wt%) were obtained from Aldrich. Thiourea (99.5%) and urea (99.5%) were purchased from Tianjin Fu Yu Chemical Co. SBA-15 (no XFF01, pore diameter: 6–10 nm, specific surface area: 550–600  $\text{m}^2 \text{g}^{-1}$ ) was bought from Jiangsu XFNANO Materials Technology Co., Ltd (Jiangsu, China). Iron chloride hexahydrate (99.9%) and ethanol (99.7%) were purchased from Adamas-beta® and

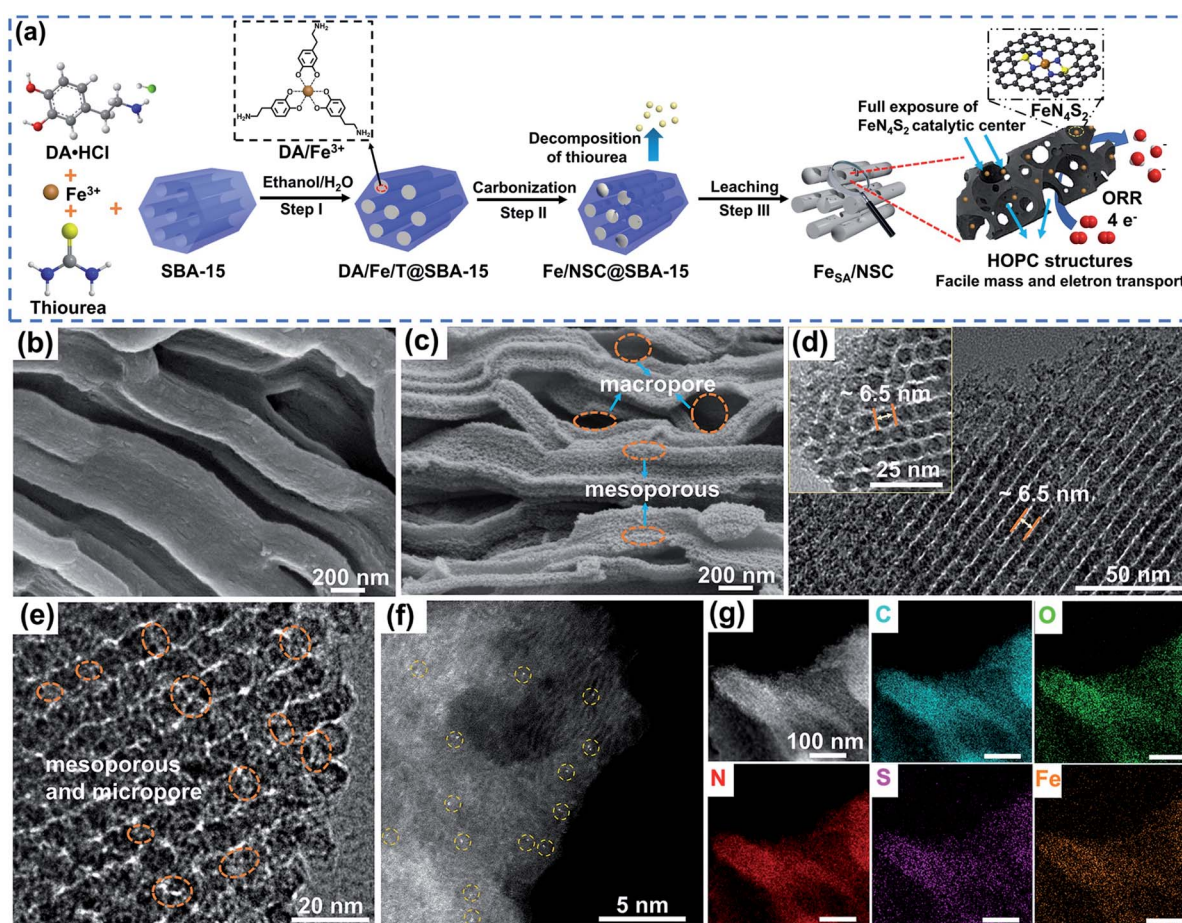


Fig. 1 (a) Schematic of the synthesis process of the  $\text{Fe}_{\text{SA}}/\text{NSC}$  catalyst. Gray, white, red, yellow, blue and orange balls represent C, H, O, S, N and Fe atoms, respectively. (b) and (c) SEM images of  $\text{Fe}/\text{NC}$  and  $\text{Fe}_{\text{SA}}/\text{NSC}$ , respectively. (d) and (e) HRTEM images of  $\text{Fe}_{\text{SA}}/\text{NSC}$ . The saffron yellow circles represent the HOPC structures. (f) HAADF-STEM image of  $\text{Fe}_{\text{SA}}/\text{NSC}$ , with single Fe atoms highlighted by yellow circles. (g) HRTEM images and corresponding elemental maps showing the elemental distribution of C (blue), O (green), N (red), S (purple) and Fe (orange).

Tianjin Fu Yu Chemical Co., respectively. All the materials were used without further purification.

## 2.2 Preparation of the catalysts

50 mg SBA-15, 100 mg dopamine hydrochloride and 200 mg thiourea were added in 15 mL ethanol and 15 mL deionized water. The resulting mixture was stirred for 30 min. Furthermore, 1 mL of  $\text{FeCl}_3 \cdot 6\text{H}_2\text{O}$  aqueous solution ( $47.5 \text{ mg mL}^{-1}$ ) was added in the mixture and the solution quickly turned dark blue, indicating the formation of an  $\text{Fe}^{3+}$ /dopamine complex. The resulting mixture was continuously stirred at  $60^\circ\text{C}$  for evaporating the solvent until the mixture became a solid. Subsequently, the obtained sample was carbonized with a two-step process under a flow of Ar in a temperature-programmable tube furnace. It was heated at  $600^\circ\text{C}$  for 60 min with a heating rate of  $2.5^\circ\text{C min}^{-1}$ , which was followed by further treatment at  $900^\circ\text{C}$  for 120 min with a heating rate of  $2^\circ\text{C min}^{-1}$ . The pyrolyzed product was treated with 4 wt% HF aqueous solution for 24 h to remove the SBA-15 template. Furthermore, the mixture was centrifuged (10 000 rpm, 5 min) and washed with deionized water several times. The obtained precipitates were leached in 2 M HCl for 24 h to remove inactive iron species. The catalyst prepared by replacing thiourea with urea in the channel of SBA-15 (called Fe/NC-UI) was prepared *via* the same procedure as above only replacing thiourea (200 mg) with urea (158 mg) with the same mole number. NSC and Fe/NC were synthesized *via* the same procedure as above without iron or thiourea, respectively. NC was synthesized *via* the same procedure as above without iron and thiourea.

Fe/NSC-TO (the catalyst prepared with thiourea outside SBA-15 channels) was prepared *via* the following procedure: 50 mg SBA-15 and 100 mg dopamine hydrochloride were added in 15 mL ethanol and 15 mL deionized water. The resulting mixture was stirred for 30 min. Furthermore, 1 mL of  $\text{FeCl}_3 \cdot 6\text{H}_2\text{O}$  aqueous solution ( $47.5 \text{ mg mL}^{-1}$ ) was added in the mixture. The resulting mixture was continuously stirred at  $60^\circ\text{C}$  for 12 h and then the solvent was slowly evaporated until the mixture became a solid. The mixture was ground and then put in the left margin of a porcelain boat. Subsequently, 200 mg thiourea was put in the right margin of the porcelain boat. The porcelain boat was put in a temperature-programmable tube furnace under a flow of Ar from right to left. Other experimental procedures followed the same steps as mentioned above.

## 2.3 Characterization

Scanning electron microscopy images were acquired on a SEM (Hitachi SU8010 Japan). Transmission electron microscopy (Hitachi HT7700 Japan) was used to observe the morphologies of the catalysts. The morphologies of the catalysts were characterized by aberration-corrected scanning transmission electron microscopy (AC-STEM) using an FEI Titan Cubed Themis G2 300 equipped with an energy dispersive X-ray spectrometer (EDS). XRD patterns at wide angles ( $10\text{--}90^\circ$ ) were collected using a Bruker D8 advanced X-ray diffractometer with Cu K $\alpha$  irradiation at 40 kV and 40 mA. X-ray photoelectron

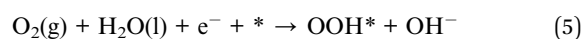
spectroscopy (XPS) was performed using an Axis Ultra spectrometer with a mono-chromatized Al K $\alpha$  X-ray as the excitation source (225 W). Brunauer–Emmett–Teller (BET) specific surface areas were measured by nitrogen adsorption–desorption analyses using a Micromeritics ASAP 2020. Raman spectra were measured on a LabRAM HR Evolution Raman microscope with 514.5 nm laser excitation in the range of  $500\text{--}2000 \text{ cm}^{-1}$ . X-ray absorption data at the Fe K-edge of the samples were recorded at room temperature in the transmission mode using ion chambers (reference samples) and fluorescence excitation mode using a Lytle detector (control samples) at beamline BL14W1 of the Shanghai Synchrotron Radiation Facility (SSRF). The station was operated with a Si(111) double crystal monochromator. During the measurements, the synchrotron was operated at 3.5 GeV and the current was between 150 and 210 mA. The data for each sample were calibrated with standard Fe metal foil. Data processing was performed using the program ATHENA. Extended X-ray absorption fine structure (EXAFS) spectra were fitted using the FEFF 6.0 code.

## 2.4 DFT calculations

The all spin-polarized density functional theory (DFT) method was employed to obtain geometric optimizations using the Vienna *ab initio* simulation package (VASP).<sup>40,41</sup> Electron exchange–correlation is represented by the Perdew–Burke–Ernzerhof (PBE) functional of generalized gradient approximation (GGA).<sup>42</sup> Projector augmented wave (PAW) pseudo-potentials were used to describe the ionic cores.<sup>43</sup> The  $\text{Fe}_{\text{SA}}/\text{NC}$  and  $\text{Fe}_{\text{SA}}/\text{NSC}$  monolayers were modeled by using a  $6 \times 6 \times 1$  supercell, and Brillouin zones were sampled with a  $2 \times 2 \times 1$  grid centered at the gamma ( $\Gamma$ ) point in the reciprocal space for geometric optimization. A vacuum region more than  $20 \text{ \AA}$  along the z-axis was set to prevent the interaction between two adjacent periodic images. A cut-off energy of 450 eV was adopted for the plane-wave basis. Van der Waals (vdW) interactions have been considered with Grimme's semiempirical DFT-D3 scheme.<sup>44</sup> Convergence tolerances for energy and force were set to  $10^{-5}$  eV and  $0.02 \text{ eV \AA}^{-1}$ , respectively. The Gibbs free energy change ( $\Delta G$ ) for each of the oxygen reduction reaction (ORR) steps was estimated by applying the computational hydrogen electrode (CHE) model of Nørskov *et al.*<sup>45</sup> The CHE model uses one half of the chemical potential of gaseous hydrogen ( $\mu(\text{H}_2)$ ) as the chemical potential of the proton–electron pair ( $\mu(\text{H}^+/e^-)$ ). The reaction scheme of the ORR in acidic media at the zero electrode potential can be written as:



In alkaline media, the elementary steps are:





According to the CHE model, the  $\Delta G$  values for each ORR step were defined as

$$\Delta G = \Delta E_{\text{DFT}} + \Delta E_{\text{ZPE}} - T\Delta S + \Delta G_{\text{U}} + \Delta G_{\text{pH}} \quad (9)$$

In this equation,  $\Delta E_{\text{DFT}}$  is the reaction energy of reactant and product molecules adsorbed on the catalyst surface, obtained from DFT calculations.  $\Delta E_{\text{ZPE}}$  and  $\Delta S$  are the change in the zero-point energy (ZPE) and entropy at room temperature ( $T = 298.15$  K), which are obtained after frequency calculations.  $\Delta G_{\text{U}}$  is the free energy contribution related to the applied electrode potential ( $U$ ).  $\Delta G_{\text{pH}}$  is the Gibbs free energy change caused by the pH value, which was calculated using

$$\Delta G_{\text{pH}} = \ln 10 \times k_{\text{B}}T \times \text{pH} \quad (10)$$

where  $k_{\text{B}}$  is the Boltzmann constant. Hence, the equilibrium potential ( $U_0$ ) for the four electron transfer ORR at pH = 0 and pH = 14 was determined to be 1.229 and 0.401 V *versus* NHE, respectively.

## 2.5 Electrochemical measurements

All of the electrochemical measurements were performed with a CHI 760E electrochemical analyzer (Cheng Hua Instruments, Inc., Shanghai, China) at room temperature. Electrochemical measurements were performed in a conventional three electrode cell by using Ag/AgCl (saturated KCl) as the reference electrode, a platinum wire as the counter electrode and catalyst coated glassy carbon (GC, 3.0 mm diameter) electrodes as the working electrodes. To prepare the working electrode, 3.0 mg of the catalyst was dispersed ultrasonically for 30 min in a solution of ethanol (600  $\mu\text{L}$ ) and Nafion (5 wt%, 30  $\mu\text{L}$ ). 10  $\mu\text{L}$  of the well-dispersed mixture was dropped onto a glassy carbon electrode with a catalyst loading of 0.674  $\text{mg cm}^{-2}$ , which was then fully dried at room temperature. Cyclic voltammetry (CV) and linear sweep voltammetry (LSV) were conducted with a sweep rate of 50  $\text{mV s}^{-1}$  and 5  $\text{mV s}^{-1}$ , respectively. All electrochemical tests were measured in  $\text{N}_2$  or  $\text{O}_2$ -saturated 0.1 M KOH aqueous solution at room temperature.

To assess the electrochemical performance of catalysts for the ORR in acidic media, suspensions of different catalysts (10  $\mu\text{L}$ ) were then dropped onto the surface of a prepolished glassy carbon electrode (GCE) followed by drying naturally. CV curves were measured in 0.1 M  $\text{HClO}_4$  with a scan rate of 50  $\text{mV s}^{-1}$ . The LSV curves for the ORR were recorded using the rotating disk electrode (RDE) technique with a scan rate of 5  $\text{mV s}^{-1}$ . The electrolyte was  $\text{N}_2$ - or  $\text{O}_2$ -saturated 0.1 M  $\text{HClO}_4$  aqueous solution.

The electron transfer number ( $n$ ) and kinetic current density ( $j_{\text{k}}$ ) were investigated based on the Koutecký–Levich (K–L) equation:

$$1/J = 1/J_{\text{K}} + 1/J_{\text{L}} = 1/B\omega^{1/2} + 1/J_{\text{K}} \quad (11)$$

$$B = 0.2nFC_0(D_0)^{2/3}\nu^{-1/6} \quad (12)$$

where  $J$  is the measured current density,  $J_{\text{K}}$  and  $J_{\text{L}}$  are the kinetic and diffusion-limiting current densities,  $\omega$  is the rotating speed of the disk,  $F$  is the Faraday constant (96 485  $\text{C mol}^{-1}$ );  $C_0$  is the bulk concentration of  $\text{O}_2$  ( $1.2 \times 10^{-6}$   $\text{mol cm}^{-3}$  in 0.1  $\text{mol L}^{-1}$  KOH and  $1.26 \times 10^{-6}$   $\text{mol cm}^{-3}$  in 0.1  $\text{mol L}^{-1}$   $\text{HClO}_4$ ),  $D_0$  is the diffusion coefficient of  $\text{O}_2$  ( $1.9 \times 10^{-5}$   $\text{cm}^2 \text{s}^{-1}$  in 0.1  $\text{mol L}^{-1}$  KOH and  $1.93 \times 10^{-5}$   $\text{cm}^2 \text{s}^{-1}$  in 0.1  $\text{mol L}^{-1}$   $\text{HClO}_4$ ); and  $\nu$  is the kinematic viscosity of the electrolyte (0.01  $\text{cm}^2 \text{s}^{-1}$  in 0.1  $\text{mol L}^{-1}$  KOH and  $1.009 \times 10^{-2}$   $\text{cm}^2 \text{s}^{-1}$  in 0.1  $\text{mol L}^{-1}$   $\text{HClO}_4$ ).

The electron transfer number and hydrogen peroxide yield ( $\%\text{H}_2\text{O}_2$ ) during the ORR can be determined by the RRDE technique:

$$\text{H}_2\text{O}_2 (\%) = (200 \times I_{\text{r}}/N)/(I_{\text{d}} + I_{\text{r}}/N) \quad (13)$$

$$n = (4 \times I_{\text{d}})/(I_{\text{d}} + I_{\text{r}}/N) \quad (14)$$

where  $I_{\text{d}}$  is the disk current,  $I_{\text{r}}$  is the ring current, and  $N = 0.37$  is the current collection efficiency of the Pt ring.

## 2.6 Zn–air battery tests

Single-cell testing of the catalyst was performed in a laboratory-constructed Zn–air battery. A polished Zn plate (purity >99.9%, thickness: 0.5 mm) was used as the anode. Homogeneous ink was loaded on 2.25  $\text{cm}^{-2}$  hydrophobic carbon paper and used as the air cathode with a loading density of 1.3  $\text{mg cm}^{-2}$ , which was dried at 60  $^\circ\text{C}$  for 12 h. In the Zn–air battery system, a microporous membrane (38  $\mu\text{m}$  polypropylene membrane, Celgard 2340, American) was used as the separator, and a nickel foam net was used as the current collector. Pictures of the detailed assembly process of the Zn–air battery are shown in Fig. S17.† For comparison, a Pt/C electrode with the same catalyst loading was also prepared.

# 3. Results and discussion

## 3.1 Synthesis and structural characterization of the catalysts

It is essential to choose appropriate precursors to anchor metal ions for constructing porous structures and finally forming single atom catalysts.<sup>11,46</sup> Polydopamine (PDA), a commonly used nitrogen-rich precursor in energy storage and conversion,<sup>47–49</sup> was first selected as a precursor complexing with metal ions to prepare porous structures by the solvent evaporation method. As shown in Fig. S1a and b,† almost no OMC structures are observed and the ferric nanoparticles appeared in the carbon framework, indicating that the insoluble and large size of the PDA/ $\text{Fe}^{3+}$  complex could restrict their infiltration into the voids of SAB-15. By contrast, OMC structures are formed in a carbon matrix by using DA as the precursor (Fig. S1c†). The as-prepared DA/ $\text{Fe}^{3+}$  complex is soluble in ethanol/water solvents, which guarantees sufficient contact with the SBA-15 template and complete filling of the channels of SBA-15. After that,

pyrocondensation polymerization of DA occurs in the channels of SBA-15 during the carbonization process. This is conducive to the formation of OMC structures and avoiding the agglomeration of Fe species during thermal pyrolysis. As shown in Fig. 1a, the mixture of the DA/Fe<sup>3+</sup> complex and thiourea infiltrated into the voids of SAB-15 by the solvent evaporation process (DA/Fe/T@SBA-15, step I). Then, decomposition of thiourea in the channels of SBA-15 occurred during the pyrolysis process in an argon atmosphere and eventually formed porous Fe based carbon materials and SBA-15 compounds (Fe/NSC@SBA-15, step II); finally, Fe<sub>SA</sub>/NSC was obtained after HF etching and acid washing (step III).

The detailed morphologies of the catalysts were observed by using scanning electron microscopy (SEM) and transmission electron microscopy (TEM) images, which show that Fe<sub>SA</sub>/NSC has HOPC structures with abundant macropores, mesopores and micropores (Fig. 1c–e) compared to Fe/NC without addition of thiourea (Fig. 1b). The different synthesis schematics of our HOPC structures (Scheme S1a†) and traditional OMC structures (Scheme S1b†) are shown in Scheme S1.† Such HOPC structures provide sufficient exposure of active sites and facilitate rapid electron transport. The catalysts prepared by replacing thiourea with urea in the channels of SBA-15 (called Fe/NC-UI) also exhibited similar HOPC structures (Fig. S2b, c and S3b†), which confirmed that the *in situ* generated gases from thiourea and urea have similar abilities to construct pore structures. Thermogravimetry (TG) technology was used to analyse the thermodecomposition process of thiourea and urea (Fig. S4†), and the results exhibited sharp decline between 200 and 400 °C. The decomposition of thiourea or urea could generate a huge amount of gases and eventually form HOPC structures *via* an *in situ* gas-foaming process. In contrast, only a small amount of HOPC structures are observed on catalyst prepared using thiourea outside SBA-15 channels (Fe/NSC-TO), Fe/NC and NC without the addition of thiourea (Fig. S2 and S3†). N<sub>2</sub> adsorption–desorption analysis was applied to further evaluate the porous structures and properties of the Fe<sub>SA</sub>/NSC, Fe/NSC-TO, Fe/NC-UI and Fe/NC catalysts (Fig. 2a). All of them display a well-defined hysteresis loop at a higher N<sub>2</sub> pressure ( $P/P_0 = 0.45–0.95$ ), suggesting the existence of mesopores.<sup>24</sup> The Brunauer–Emmett–Teller (BET) surface area and the total pore volume of Fe<sub>SA</sub>/NSC are measured to be 1224.03 m<sup>2</sup> g<sup>-1</sup> and 1.7 cm<sup>3</sup> g<sup>-1</sup>, which are much larger than those of Fe/NSC-TO (704.64 m<sup>2</sup> g<sup>-1</sup> and 0.8 cm<sup>3</sup> g<sup>-1</sup>), Fe/NC-UI (1091.34 m<sup>2</sup> g<sup>-1</sup> and 1.37 cm<sup>3</sup> g<sup>-1</sup>), and Fe/NC (858.92 m<sup>2</sup> g<sup>-1</sup> and 0.7 cm<sup>3</sup> g<sup>-1</sup>). Moreover, Fe<sub>SA</sub>/NSC and Fe/NC-UI catalysts exhibit a wider pore size distribution (PSD) than Fe/NSC-TO and Fe/NC (Fig. 2b), and could be classified into three levels: (1) porous carbon skeletons (50–200 nm) with massive macropores; (2) abundant mesopores mainly concentrated at about 6.5 nm; and (3) a large number of micropores (<2 nm) throughout the entire structure. By contrast, the PSDs of Fe/NSC-TO and Fe/NC were mainly centered at about 6.5 nm, revealing the existence of a single PSD without addition of thiourea or urea, further strengthening the role of thiourea or urea in constructing HOPC structures.

To further demonstrate the existential state of ferric species, Fe<sub>SA</sub>/NSC was characterized by high-angle annular dark-field

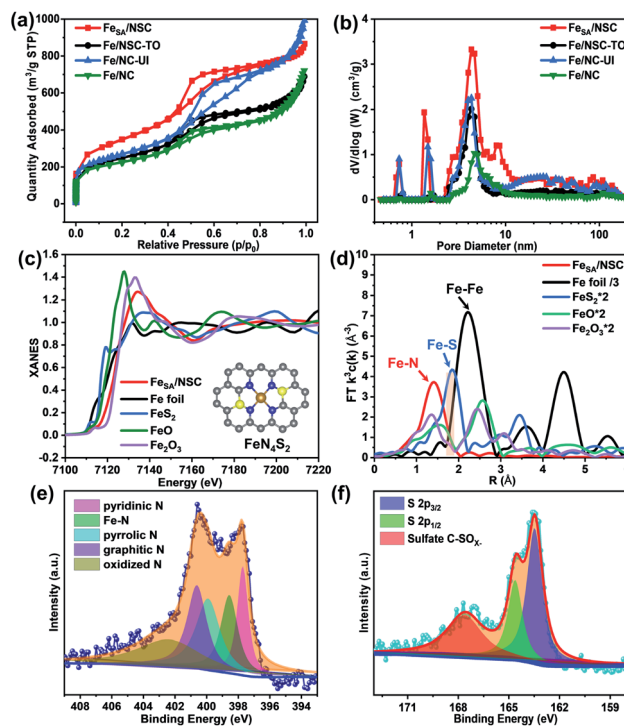


Fig. 2 (a) Nitrogen adsorption–desorption isotherm spectra and (b) pore size distribution (PSD) curves of Fe<sub>SA</sub>/NSC, Fe/NSC-TO, Fe/NC-UI, and Fe/NC. (c) Fe K-edge X-ray absorption near-edge structure (XANES) and (d) Fourier transform-extended X-ray absorption fine structure (FT-EXAFS) spectra of Fe<sub>SA</sub>/NSC, Fe foil, FeS<sub>2</sub>, FeO, and Fe<sub>2</sub>O<sub>3</sub>. Inset in (c): model of FeN<sub>4</sub>S<sub>2</sub>; Fe orange sphere, N blue spheres, S yellow spheres and C gray spheres. High-resolution XPS spectra of N 1s (e) and (f) S 2p of Fe<sub>SA</sub>/NSC.

scanning transmission electron microscopy (HAADF-STEM), which shows that Fe species are atomically dispersed on the carbon support (marked with yellow circles) (Fig. 1f). No aggregated metallic species are observed in high-resolution transmission electron microscopy (HRTEM) (Fig. 1d and e). Energy dispersive X-ray spectroscopy (EDS) mapping images reveal that Fe, N, S, O, and C are uniformly distributed throughout the entire nanostructure of the Fe<sub>SA</sub>/NSC catalyst. The X-ray absorption near edge structure (XANES) spectra of Fe<sub>SA</sub>/NSC in Fig. 2c reveal that the absorption edge position is located between those of FeO and Fe<sub>2</sub>O<sub>3</sub>, reflecting that the valence state of Fe species in Fe<sub>SA</sub>/NSC is between Fe<sup>2+</sup> and Fe<sup>3+</sup>.<sup>50</sup> The main peak around 1.5 Å is observed in the Fourier transform (FT)  $k^3$ -weighted extended X-ray absorption fine structure (EXAFS) spectrum of Fe<sub>SA</sub>/NSC, attributable to the Fe–N coordination in the structure.<sup>23,51</sup> No characteristic peaks of Fe–Fe at about 2.2 Å and Fe–S at about 1.8 Å for Fe<sub>SA</sub>/NSC are observed, further indicating that Fe atoms are dispersed on the HOPC framework and stabilized by nitrogen. To further identify the local structural parameters of Fe atoms in Fe<sub>SA</sub>/NSC, quantitative EXAFS fitting was conducted (Fig. S6c†). EXAFS fitting parameters listed in Table S2† evidence that the Fe atoms in Fe<sub>SA</sub>/NSC are coordinated by four N atoms with two sets of Fe–N bond lengths (1.98 Å and 1.87 Å). This is attributed to the

doping of S that plays a role in influencing the Fe–N bond length.<sup>33</sup> An accurate model of FeN<sub>4</sub>S<sub>2</sub> active sites on the HOPC carbon framework was deduced using density functional theory (DFT). Among the four feasible structures of FeN<sub>4</sub>S<sub>2</sub> active sites (Fig. S7†), the most possible structure was found (Fig. S7b†), which reveals very close structural parameters with those obtained from experimental measurements (Tables S2 and S3†). Therefore, the centre site of FeN<sub>4</sub>S<sub>2</sub> (inset in Fig. 2c) dominates the Fe<sub>SA</sub>/NSC catalyst.

To gain deep insight into the surface chemical composition and elemental bonding configuration of the catalysts, X-ray photoelectron spectroscopy (XPS) analyses were conducted, which reveal that C, N, O, S and Fe elements are included in Fe<sub>SA</sub>/NSC (Fig. S8a†), and no Si 2p signal is observed in the XPS spectra of the catalysts, indicating the complete removal of SBA-15 templates by HF. As shown in Fig. 2e, high-resolution N 1s spectra of Fe<sub>SA</sub>/NSC can be fitted to five peaks, pyridinic N at 397.8 eV, Fe–N<sub>x</sub> at 398.6 eV, pyrrolic N at 399.9 eV, graphitic N at 400.7 eV and oxidized N at 402.4 eV. Along with S doping, the high resolution S 2p spectra in Fig. 2f highlight two main peaks corresponding to the binding energies of 163.9 eV, 164.9 eV assigned to S 2p<sub>3/2</sub> and S 2p<sub>1/2</sub> of the thiophene-like structure (C–S–C) between carbon and sulfur atoms, respectively.<sup>52</sup> A small peak at around 167.6 eV is also observed, corresponding to the sulfate species. No metal–S bonds are detected for Fe<sub>SA</sub>/NSC in either Fe 2p or S 2p spectra, further reflecting that Fe species are only anchored with N. The high-resolution Fe 2p XPS spectra show that no signals of metallic Fe are detected in Fe<sub>SA</sub>/NSC (Fig. S8c†). However, metallic Fe appeared in the Fe 2p XPS spectrum of Fe/NC without the addition of thiourea or urea (Fig. S8c†), suggesting that thiourea or urea plays an important role in providing a N source and anchoring Fe atoms. The contents of sulfur for Fe<sub>SA</sub>/NSC, Fe/NSC-TO and NSC are 1.42, 1.28 and 1.36 at% based on XPS analysis, respectively (Table S4†). The amount of Fe coordinated to N on Fe<sub>SA</sub>/NSC samples obtained from inductively coupled plasma atomic emission spectroscopic (ICP-AES) measurements is 1.22 wt% (Table S5†). X-ray diffraction (XRD) was conducted to analyse the iron and carbon crystalline structures of the catalysts. From Fig. S9a,† two characteristic peaks at 25° and 44° are observed in the XRD patterns of Fe<sub>SA</sub>/NSC, Fe/NSC-TE, Fe/NC-UI, Fe/NC, NSC and NC, indicating successful carbonization after pyrolysis. Notably, no diffraction peaks of crystalline Fe species are observed from the XRD patterns of Fe<sub>SA</sub>/NSC, Fe/NSC-TO, and Fe/NC-UI.

### 3.2 ORR performances of the catalysts

After structural and compositional characterization, the electrocatalytic property measurements of as-obtained catalysts were further explored. Cyclic voltammetry (CV) was first conducted for catalysts in N<sub>2</sub>- and O<sub>2</sub>-saturated 0.1 M KOH electrolytes (Fig. S10b†). No distinctly featured peaks emerge in the N<sub>2</sub>-saturated solution. By contrast, all the catalysts exhibit a well-defined ORR peak between 0.75 and 0.90 V, indicating their ORR catalytic capability in 0.1 M KOH. Among them, the Fe<sub>SA</sub>/NSC catalyst shows the most positive ORR peak potential, which is 25 mV larger than that of the Pt/C catalyst (Fig. S10†).

Moreover, the linear sweep voltammetry (LSV) curves were measured on a rotating ring electrode (RDE) in O<sub>2</sub>-saturated 0.1 M KOH. As revealed in Fig. 3a and b, the Fe<sub>SA</sub>/NSC catalyst shows the most excellent ORR performance with a positive half-wave potential ( $E_{1/2}$ ) of 0.91 V and the highest diffusion kinetic current density ( $J_k$ ) at 19.83 mA cm<sup>-2</sup>, among all the catalysts investigated in this work (Fe/NSC-TO,  $E_{1/2}$  = 0.87 V,  $J_k$  = 15.48 mA cm<sup>-2</sup>; Fe/NC-UI,  $E_{1/2}$  = 0.86 V,  $J_k$  = 13.28 mA cm<sup>-2</sup>; Fe/NC,  $E_{1/2}$  = 0.83 V,  $J_k$  = 6.07 mA cm<sup>-2</sup>; NSC,  $E_{1/2}$  = 0.80 V,  $J_k$  = 1.36 mA cm<sup>-2</sup>; NC,  $E_{1/2}$  = 0.77 V,  $J_k$  = 0.40 mA cm<sup>-2</sup>). The results demonstrate that HOPC structures and the introduction of S into Fe<sub>SA</sub>/NSC catalysts contribute to the improvement of ORR activity. The  $E_{1/2}$  and  $J_k$  of Fe<sub>SA</sub>/NSC are even much better than those of commercial Pt/C ( $E_{1/2}$  = 0.87 V,  $J_k$  = 17.41 mA cm<sup>-2</sup>) (Fig. 3b). The ORR catalytic activity of Fe<sub>SA</sub>/NSC is higher than those of most recently reported Fe-based electrocatalysts or other non-precious M–N/C catalysts (Table S6†). To quantify the ORR pathway, the rotating ring-disk electrode (RRDE) method was used to monitor the yield of H<sub>2</sub>O<sub>2</sub> during the ORR process. The H<sub>2</sub>O<sub>2</sub> yield of Fe<sub>SA</sub>/NSC is below 5% in the potential range of 0.2 to 0.7 V, indicating the superior selectivity toward H<sub>2</sub>O

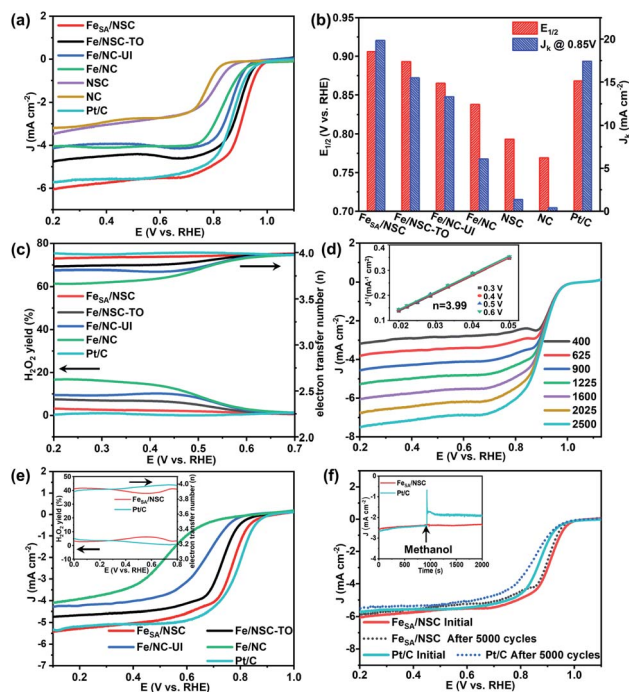


Fig. 3 (a) LSV curves of Fe<sub>SA</sub>/NSC, Fe/NSC-TO, Fe/NC-UI, Fe/NC, NSC, NC and Pt/C catalysts in O<sub>2</sub>-saturated 0.1 M KOH with a rotation rate of 1600 rpm. (b) Comparison of  $E_{1/2}$  and the kinetic current density ( $J_k$ ) at 0.85 V (vs. RHE) for various catalysts. (c) H<sub>2</sub>O<sub>2</sub> yields and electron transfer numbers ( $n$ ) of different catalysts in O<sub>2</sub>-saturated 0.1 M KOH solution. (d) ORR polarization curves of Fe<sub>SA</sub>/NSC at different rotating rates (inset: K–L plots and electron transfer numbers). (e) LSV voltammograms of various catalysts in O<sub>2</sub>-saturated 0.1 M HClO<sub>4</sub> with a rotation rate of 1600 rpm. (f) ORR polarization curves of Fe<sub>SA</sub>/NSC and Pt/C before and after 5000 potential cycles over 0.8–1.1 V with a sweep rate of 100 mV s<sup>-1</sup> in O<sub>2</sub>-saturated 0.1 M KOH. Inset: chronoamperometric responses of different catalysts in 0.1 M KOH before and after adding 0.5 M methanol.

during the ORR process. The electron transfer number of  $\text{Fe}_{\text{SA}}/\text{NSC}$  is between 3.92 and 3.99 V from 0.2–0.7 V, evidencing that  $\text{Fe}_{\text{SA}}/\text{NSC}$  undergoes a four-electron process during oxygen reduction. It is much higher than those of other catalysts:  $\text{Fe}/\text{NSC-TO}$  (3.84–3.98),  $\text{Fe}/\text{NC-UI}$  (3.81–3.98), and  $\text{Fe}/\text{NC}$  (3.67–3.97) (Fig. 3c). RDE measurements with rotating speeds ranging from 400 to 2500 rpm were used to analyze ORR kinetics and selectivity (Fig. 3d). The limited current density of  $\text{Fe}_{\text{SA}}/\text{NSC}$  increases uniformly with the increase of the rotating speed; K–L plots exhibit a good linear relationship and the average electron transfer number ( $n$ ) is 3.99, indicating a direct four-electron pathway for the ORR. Among the catalysts,  $\text{Fe}_{\text{SA}}/\text{NSC}$  shows the smallest Nyquist circle in electrochemical impedance spectroscopy (EIS) compared with other catalysts (Fig. S12a†), which demonstrated the quickest charge transfer ability. Furthermore,  $\text{Fe}_{\text{SA}}/\text{NSC}$  shows a lower Tafel slope ( $55.9 \text{ mV dec}^{-1}$ ) than the Pt/C electrode ( $67.1 \text{ mV dec}^{-1}$ ) in the low overpotential region (Fig. S12b†). It is further found that the ORR performances of the catalysts in acidic solutions follow the same trend as those in alkaline electrolytes:  $\text{Fe}_{\text{SA}}/\text{NSC} > \text{Fe}/\text{NSC-TO} > \text{Fe}/\text{NC-UI} > \text{Fe}/\text{NC}$ . LSV curves in  $\text{O}_2$ -saturated 0.1 M  $\text{HClO}_4$  are shown in Fig. 3e.  $\text{Fe}_{\text{SA}}/\text{NSC}$  still exhibits a higher ORR activity ( $E_{1/2} = 0.78 \text{ V}$ ) than  $\text{Fe}/\text{NSC-TO}$  ( $E_{1/2} = 0.75 \text{ V}$ ) and  $\text{Fe}/\text{NC-UI}$  ( $E_{1/2} = 0.69 \text{ V}$ ), and is even comparable to the commercial Pt/C catalyst ( $E_{1/2} = 0.84 \text{ V}$ ). Moreover, the  $\text{H}_2\text{O}_2$  yield of  $\text{Fe}_{\text{SA}}/\text{NSC}$  is below 6.2% in the potential range of 0 to 0.8 V, indicating the excellent 4-electron selectivity of the ORR in 0.1 M  $\text{HClO}_4$ . The electron transfer number of  $\text{Fe}_{\text{SA}}/\text{NSC}$  in 0.1 M  $\text{HClO}_4$  is between 3.88 and 3.95 from 0 to 0.8 V (inset in Fig. 3e), suggesting a direct 4-electron transfer pathway. The excellent catalytic activity of  $\text{Fe}_{\text{SA}}/\text{NSC}$  could result from the synergetic effect of the high exposure of active sites and efficient mass transfer through HOPC structures. In addition, the introduction of S can also improve the overall ORR efficiency. To understand the origin of the ORR activity of  $\text{Fe}_{\text{SA}}/\text{NSC}$ , 10 mM  $\text{SCN}^-$  was used as a probe to poison  $\text{Fe-N}_4$  sites for the ORR in 0.1 M KOH. As revealed in Fig. S13,† the  $E_{1/2}$  of  $\text{Fe}_{\text{SA}}/\text{NSC}$  decreased dramatically by about 50 mV. The result suggests that single Fe atoms in  $\text{Fe}_{\text{SA}}/\text{NSC}$  catalysts play a leading role in improving ORR activity. Moreover, after increasing the concentration of  $\text{SCN}^-$  to 20 mM and 40 mM, the LSV curves don't show any obvious change (Fig. S13†), indicating that nearly all Fe sites have been blocked. However, the  $E_{1/2}$  value is still much larger than that of pure  $\text{SCN}$  catalysts without Fe. The studies demonstrate that Fe sites in the  $\text{Fe}_{\text{SA}}/\text{NSC}$  catalyst are not the sole reason for the better ORR activity, the Fe sites may also activate the surrounding coordinated atoms and render them active.<sup>53</sup>

For practical applications of single atom catalysts, ORR catalytic stability and selectivity for the ORR are two major factors that should be considered.<sup>54</sup> In this work, the durability of catalysts was evaluated by chronoamperometric measurements. As shown in Fig. 3f, the  $E_{1/2}$  of the  $\text{Fe}_{\text{SA}}/\text{NSC}$  exhibits a 3 mV negative shift after 5000 potential cycles in 0.1 M KOH. By contrast, the  $E_{1/2}$  of the Pt/C shows a 12 mV negative shift after 5000 potential cycles in 0.1 M KOH, indicating the better stability of  $\text{Fe}_{\text{SA}}/\text{NSC}$  than the commercial Pt/

C catalyst. Meanwhile, it also exhibits better stability in 0.1 M  $\text{HClO}_4$ , and the  $E_{1/2}$  of the  $\text{Fe}_{\text{SA}}/\text{NSC}$  catalyst decays by only 8 mV after 5000 CV cycles between 0.6 and 1.0 V, which is lower than that of the Pt/C catalyst (16 mV) (Fig. S16†). The resistance to methanol was investigated by adding 0.5 M methanol into the electrolyte for about 1000 s during chronoamperometric measurements (inset picture in Fig. 3f and S16†). It shows only a slight oscillation in the current, implying a great methanol tolerance in both alkaline and acidic electrolytes. In contrast, the current of the Pt/C catalyst exhibits drastic fluctuation after 0.5 M methanol injection. The results demonstrate that  $\text{Fe}_{\text{SA}}/\text{NSC}$  has better stability and methanol resistance than the Pt/C catalyst in both alkaline and acidic media, making it a promising candidate for application in practical energy devices.

### 3.3 Electrochemical performance of Zn–air batteries with $\text{Fe}_{\text{SA}}/\text{NSC}$

Zinc–air batteries are promising energy devices in energy conversion and storage.<sup>55,56</sup> To estimate the potential application of the  $\text{Fe}_{\text{SA}}/\text{NSC}$  electrocatalyst in energy devices, a Zn–air battery was further tested using  $\text{Fe}_{\text{SA}}/\text{NSC}$  as the oxygen electrocatalyst (Fig. 4a). It shows an open-circuit voltage of 1.501 V

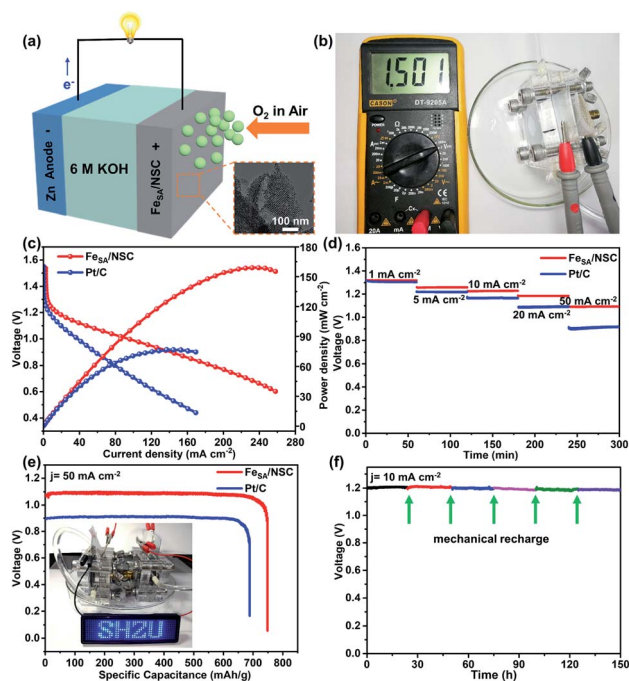


Fig. 4 (a) Schematic diagram of the Zn–air battery. (b) Photograph of the Zn–air battery with an open-circuit voltage of 1.501 V. (c) Discharge polarization curves and corresponding power density plots of Zn–air batteries using  $\text{Fe}_{\text{SA}}/\text{NSC}$  and Pt/C as air electrodes, respectively. (d) Discharge curves of the batteries at various current densities. (e) Specific capacities of Zn–air batteries using  $\text{Fe}_{\text{SA}}/\text{NSC}$  and Pt/C as ORR catalysts. Long time galvanostatic discharge curves of the Zn–air batteries at  $50 \text{ mA cm}^{-2}$ . Inset: photograph of two Zn–air batteries lighting up an LED. (f) Stability of the Zn–air battery with  $\text{Fe}_{\text{SA}}/\text{NSC}$  as the cathode catalyst by replenishing the electrolyte and Zn anode at  $10 \text{ mA cm}^{-2}$ .

(Fig. 4b), which is close to the theoretical value of 1.65 V. The Fe<sub>SA</sub>/NSC-assembled Zn-air battery exhibits a maximum power density of 159.2 mW cm<sup>-2</sup> at a current density of 235.6 mA cm<sup>-2</sup> (Fig. 4c), which are much higher than those of the Pt/C-assembled Zn-air battery (76.8 mW cm<sup>-2</sup> at 151.7 mA cm<sup>-2</sup>) and those of other previously reported oxygen electrocatalysts, e.g., N, P-doped carbon foam (55 mW cm<sup>-2</sup>),<sup>57</sup> Fe-N/P-C-700 (133.2 mW cm<sup>-2</sup>),<sup>50</sup> and 2D mesoporous FeCo-N-x-carbon (150 mW cm<sup>-2</sup>).<sup>58</sup> The galvanostatic discharge curves for the Fe<sub>SA</sub>/NSC based Zn-air battery show superior discharge stabilities and higher voltage values at various current densities ranging from 1 to 50 mA cm<sup>-2</sup> (Fig. 4d). A blue light-emitting diode (LED) screen with the letters of SHZU can be easily powered by two Fe<sub>SA</sub>/NSC-assembled batteries connected in series (inset in Fig. 4e). The galvanostatic discharge curve of an Fe<sub>SA</sub>/NSC based battery exhibits a stable discharge voltage at about 1.1 V with no obvious degradation at 50 mA cm<sup>-2</sup> (Fig. 4e), which is much higher than that of a Pt/C-assembled battery (about 0.92 V). The specific capacity for the Fe<sub>SA</sub>/NSC-equipped battery at 50 mA cm<sup>-2</sup> is 748.4 mA h g<sup>-1</sup>, which is larger than that of a commercial Pt/C-assembled battery (688.6 mA h g<sup>-1</sup>). Notably, no obvious degradation is observed after 6 cycles for about 150 hours by replenishing the electrolyte and Zn anode (Fig. 4f), indicating the outstanding durability of the Fe<sub>SA</sub>/NSC catalyst in Zn-air batteries. Such an excellent performance demonstrates again the outstanding catalytic activity and stability of Fe<sub>SA</sub>/NSC for the ORR.

### 3.4 Theoretical evaluation of ORR activities

To gain theoretical insights into S-doping on Fe<sub>SA</sub>/NSC for high ORR reactivity and excellent ORR kinetics, DFT calculations were employed to illustrate the changes in reaction energy and electronic structure before and after S-doping

(Fig. 5a under acidic conditions and Fig. S19† under alkaline conditions). As shown in Fig. 5a and b, the last step of the ORR is the most endothermic and thus is the rate determining step (RDS) for both catalysts. The  $\Delta G$  of the RDS for Fe<sub>SA</sub>/NSC (0.58 eV) is smaller than that for Fe<sub>SA</sub>/NC (0.69 eV) at equilibrium potential. It indicates that Fe<sub>SA</sub>/NSC is more effective for the ORR than Fe<sub>SA</sub>/NC, indicating a better ORR performance after S modification. The differential charge density maps (Fig. 5d and e) show that more electrons would accumulate on O<sub>2</sub> (0.53 e) when adsorbed on the Fe<sub>SA</sub>/NSC structure compared with the Fe<sub>SA</sub>/NC structure (0.50 e), which is beneficial for the reduction of O<sub>2</sub>.<sup>59</sup> Furthermore, the charge density differences and Bader charge analysis (Fig. S20†) reveal that S doping can tune the charge of Fe through the atomic interface effectively, which makes Fe in Fe<sub>SA</sub>/NSC less positive than in Fe<sub>SA</sub>/NC (1.07 for Fe<sub>SA</sub>/NC and 1.01 for Fe<sub>SA</sub>/NSC). The relatively low electronegativity of S could enrich the charge around the N atom. It promotes the rate-limiting reductive release of OH\*, reduces the reaction barrier and facilitates the overall ORR process.<sup>60</sup> Therefore, the excellent ORR activity in both alkaline and acid solutions resulting from S doping enables the engineering of charges on the Fe reactive center and HOPC structures (facilitating active site access and mass transfer).

## 4. Conclusions

In summary, a facile *in situ* gas-foaming strategy was developed to synthesize single Fe atoms dispersed on a N, S-codoped hierarchically ordered porous carbon framework by one-step pyrolysis of dopamine/ferric chloride complexes and thiourea confined within the channels of SBA-15. HOPC structures can facilitate active site access and mass transfer in the ORR process. The introduction of S can induce charge enrichment in N and Fe for optimal O<sub>2</sub> binding and fast electron transfer, which make them exhibit superb oxygen reduction activity, stability and methanol tolerance in both acidic and alkaline media. As the air electrode in Zn-air batteries, Fe<sub>SA</sub>/NSC demonstrates superior power density, long-term discharge stability and specific capacity to the commercial Pt/C catalyst. Therefore, the Fe<sub>SA</sub>/NSC catalyst is a promising non-platinum-group metal ORR catalyst for practical application in Zn-air batteries.

## Conflicts of interest

There are no conflicts to declare.

## Acknowledgements

This study was supported by the National Natural Science Foundation of China (U1703351, 52073179 and 51663021), Bingtuan Excellent Young Scholars (CZ027205), Bingtuan Science & Technology Nova Program and Postgraduate Education Innovation Program of Xinjiang Uygur Autonomous Region in 2021. We wish to thank the Analysis and Testing Center of

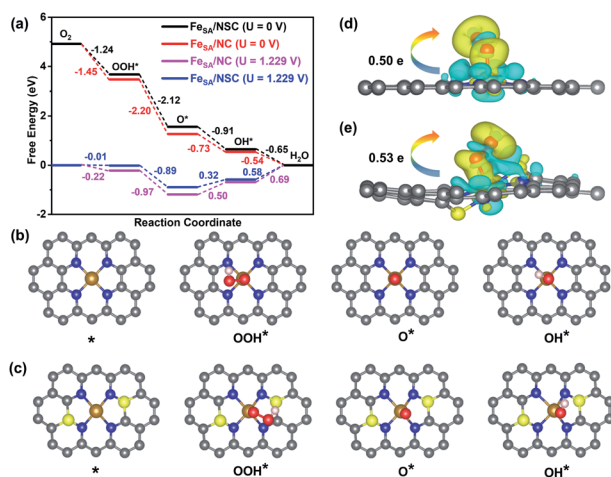


Fig. 5 The Gibbs free energy diagram of the ORR on (a) Fe<sub>SA</sub>/NC and Fe<sub>SA</sub>/NSC obtained from DFT calculations. The optimized structures of the intermediates of the ORR on (b) Fe<sub>SA</sub>/NC and (c) Fe<sub>SA</sub>/NSC. Gray, white, red, yellow, blue and gold balls represent C, H, O, S, N and Fe atoms, respectively. (d) Differential charge density and Bader charge analysis of O<sub>2</sub> adsorbed on (d) Fe<sub>SA</sub>/NC and (e) Fe<sub>SA</sub>/NSC sites. Electron accumulation is shown in yellow and depletion in blue.

Shihezi University for the microscopy experiments and micro-analysis of our specimens.

## Notes and references

- G. Wu, K. L. More, C. M. Johnston and P. Zelenay, *Science*, 2011, **332**, 443–447.
- L. Zhang, J. M. T. A. Fischer, Y. Jia, X. Yan, W. Xu, X. Wang, J. Chen, D. Yang, H. Liu, L. Zhuang, M. Hanke, D. J. Searles, K. Huang, S. Feng, C. L. Brown and X. Yao, *J. Am. Chem. Soc.*, 2018, **140**, 10757–10763.
- W.-T. Wang, N. Batool, T.-H. Zhang, J. Liu, X.-F. Han, J.-H. Tian and R. Yang, *J. Mater. Chem. A*, 2021, **9**, 3952–3960.
- W. Y. Noh, E. M. Kim, K. Y. Kim, J. H. Kim, H. Y. Jeong, P. Sharma, G. Lee, J.-W. Jang, S. H. Joo and J. S. Lee, *J. Mater. Chem. A*, 2020, **8**, 18891–18902.
- P. Chen, T. Zhou, L. Xing, K. Xu, Y. Tong, H. Xie, L. Zhang, W. Yan, W. Chu, C. Wu and Y. Xie, *Angew. Chem., Int. Ed.*, 2017, **56**, 610–614.
- H.-W. Liang, W. Wei, Z.-S. Wu, X. Feng and K. Müllen, *J. Am. Chem. Soc.*, 2013, **135**, 16002–16005.
- J. Li, M. Chen, D. A. Cullen, S. Hwang, M. Wang, B. Li, K. Liu, S. Karakalos, M. Lucero, H. Zhang, C. Lei, H. Xu, G. E. Sterbinsky, Z. Feng, D. Su, K. L. More, G. Wang, Z. Wang and G. Wu, *Nat. Catal.*, 2018, **1**, 935–945.
- L. Li, J. He, Y. Wang, X. Lv, X. Gu, P. Dai, D. Liu and X. Zhao, *J. Mater. Chem. A*, 2019, **7**, 1964–1988.
- Z. Jiang, W. Sun, H. Shang, W. Chen, T. Sun, H. Li, J. Dong, J. Zhou, Z. Li, Y. Wang, R. Cao, R. Sarangi, Z. Yang, D. Wang, J. Zhang and Y. Li, *Energy Environ. Sci.*, 2019, **12**, 3508–3514.
- A. Garcia, M. Retuerto, C. Dominguez, L. Pascual, P. Ferrer, D. Gianolio, A. Serrano, P. Assmann, D. G. Sanchez, M. A. Pena and S. Rojas, *Appl. Catal., B*, 2020, **278**, 119270.
- Y. Chen, S. Ji, C. Chen, Q. Peng, D. Wang and Y. Li, *Joule*, 2018, **2**, 1242–1264.
- H. Yang, Z. Li, S. Kou, G. Lu and Z. Liu, *Appl. Catal., B*, 2020, **278**, 119270.
- Y. Peng, B. Lu and S. Chen, *Adv. Mater.*, 2018, **30**, 1801995.
- D. U. Lee, P. Xu, Z. P. Cano, A. G. Kashkooli, M. G. Park and Z. Chen, *J. Mater. Chem. A*, 2016, **4**, 7107–7134.
- H. Zhang, W. Zhou, T. Chen, B. Y. Guan, Z. Li and X. W. Lou, *Energy Environ. Sci.*, 2018, **11**, 1980–1984.
- S. Chen, N. Zhang, C. W. Narváez Villarrubia, X. Huang, L. Xie, X. Wang, X. Kong, H. Xu, G. Wu, J. Zeng and H.-L. Wang, *Nano Energy*, 2019, **66**, 104164.
- U. Martinez, S. Komini Babu, E. F. Holby, H. T. Chung, X. Yin and P. Zelenay, *Adv. Mater.*, 2019, **31**, 1806545.
- Y. Deng, B. Chi, X. Tian, Z. Cui, E. Liu, Q. Jia, W. Fan, G. Wang, D. Dang, M. Li, K. Zang, J. Luo, Y. Hu, S. Liao, X. Sun and S. Mukerjee, *J. Mater. Chem. A*, 2019, **7**, 5020–5030.
- P. Peng, L. Shi, F. Huo, C. Mi, X. Wu, S. Zhang and Z. Xiang, *Sci. Adv.*, 2019, **5**, eaaw2322.
- Y. Han, Y. Wang, R. Xu, W. Chen, L. Zheng, A. Han, Y. Zhu, J. Zhang, H. Zhang, J. Luo, C. Chen, Q. Peng, D. Wang and Y. Li, *Energy Environ. Sci.*, 2018, **11**, 2348–2352.
- R. Cao, R. Thapa, H. Kim, X. Xu, M. Gyu Kim, Q. Li, N. Park, M. Liu and J. Cho, *Nat. Commun.*, 2013, **4**, 2076.
- L. Jiao, G. Wan, R. Zhang, H. Zhou, S.-H. Yu and H.-L. Jiang, *Angew. Chem., Int. Ed.*, 2018, **57**, 8525–8529.
- Z. Zhang, J. Sun, F. Wang and L. Dai, *Angew. Chem., Int. Ed.*, 2018, **57**, 9038–9043.
- G. Chen, P. Liu, Z. Liao, F. Sun, Y. He, H. Zhong, T. Zhang, E. Zschech, M. Chen, G. Wu, J. Zhang and X. Feng, *Adv. Mater.*, 2020, **32**, 1907399.
- Q. Li, W. Chen, H. Xiao, Y. Gong, Z. Li, L. Zheng, X. Zheng, W. Yan, W. C. Cheong, R. Shen, N. Fu, L. Gu, Z. Zhuang, C. Chen, D. Wang, Q. Peng, J. Li and Y. Li, *Adv. Mater.*, 2018, **30**, 1800588.
- X. Han, X. Ling, D. Yu, D. Xie, L. Li, S. Peng, C. Zhong, N. Zhao, Y. Deng and W. Hu, *Adv. Mater.*, 2019, **31**, 1905622.
- Z. Lu, B. Wang, Y. Hu, W. Liu, Y. Zhao, R. Yang, Z. Li, J. Luo, B. Chi, Z. Jiang, M. Li, S. Mu, S. Liao, J. Zhang and X. Sun, *Angew. Chem., Int. Ed.*, 2019, **58**, 2622–2626.
- R. Zhao, Z. Liang, S. Gao, C. Yang, B. Zhu, J. Zhao, C. Qu, R. Zou and Q. Xu, *Angew. Chem., Int. Ed.*, 2019, **58**, 1975–1979.
- L. Jiao, G. Wan, R. Zhang, H. Zhou, S. H. Yu and H. L. Jiang, *Angew. Chem., Int. Ed.*, 2018, **57**, 8525–8529.
- A. Kong, X. Zhu, Z. Han, Y. Yu, Y. Zhang, B. Dong and Y. Shan, *ACS Catal.*, 2014, **4**, 1793–1800.
- Y. Shi, Y. Wan, R. Zhang and D. Zhao, *Adv. Funct. Mater.*, 2008, **18**, 2436–2443.
- Z. K. Yang, C.-Z. Yuan and A.-W. Xu, *ACS Energy Lett.*, 2018, **3**, 2383–2389.
- Q. Li, W. Chen, H. Xiao, Y. Gong, Z. Li, L. Zheng, X. Zheng, W. Yan, W.-C. Cheong, R. Shen, N. Fu, L. Gu, Z. Zhuang, C. Chen, D. Wang, Q. Peng, J. Li and Y. Li, *Adv. Mater.*, 2018, **30**, 1800588.
- J. Zhang, Y. Zhao, C. Chen, Y.-C. Huang, C.-L. Dong, C.-J. Chen, R.-S. Liu, C. Wang, K. Yan, Y. Li and G. Wang, *J. Am. Chem. Soc.*, 2019, **141**, 20118–20126.
- Y. Hou, M. Qiu, M. G. Kim, P. Liu, G. Nam, T. Zhang, X. Zhuang, B. Yang, J. Cho, M. Chen, C. Yuan, L. Lei and X. Feng, *Nat. Commun.*, 2019, **10**, 1392.
- Z. Zhu, H. Yin, Y. Wang, C. H. Chuang, L. Xing, M. Dong, Y. R. Lu, G. Casillas-Garcia, Y. Zheng, S. Chen, Y. Dou, P. Liu, Q. Cheng and H. Zhao, *Adv. Mater.*, 2020, **32**, 2004670.
- M. Qiao, Y. Wang, Q. Wang, G. Hu, X. Mamat, S. Zhang and S. Wang, *Angew. Chem., Int. Ed.*, 2020, **59**, 2688–2694.
- X. Liu, J. Kang, Y. Dai, C. Dong, X. Guo and X. Jia, *Adv. Mater. Interfaces*, 2018, **5**, 1800303.
- X. Chen, W. Dong, Y. Yao, L. Li, W. Hua, G. Zhuang, D. Zhao, S. Yan and W. Song, *Appl. Catal., B*, 2020, **269**, 118756.
- G. Kresse, *Phys. Rev. B: Condens. Matter Mater. Phys.*, 1996, **54**, 11169–11186.
- G. Kresse and D. Joubert, *Phys. Rev. B: Condens. Matter Mater. Phys.*, 1999, **59**, 1758–1775.
- J. P. Perdew, K. Burke and M. Ernzerhof, *Phys. Rev. Lett.*, 1996, **77**, 3865.
- G. Kresse and D. Joubert, *Phys. Rev. B: Condens. Matter Mater. Phys.*, 1999, **59**, 1758.

- 44 S. Grimme, J. Antony, S. Ehrlich and H. Krieg, *J. Chem. Phys.*, 2010, **132**, 154104.
- 45 A. A. Peterson, F. Abild-Pedersen, F. Studt, J. Rossmeisl and J. K. Nørskov, *Energy Environ. Sci.*, 2010, **3**, 1311–1315.
- 46 Y. Lin, P. Liu, E. Velasco, G. Yao, Z. Tian, L. Zhang and L. Chen, *Adv. Mater.*, 2019, **31**, 1808193.
- 47 W. Wei, H. Liang, K. Parvez, X. Zhuang, X. Feng and K. Mullen, *Angew. Chem., Int. Ed.*, 2014, **53**, 1570–1574.
- 48 Z. Wang, Y. Zou, Y. Li and Y. Cheng, *Small*, 2020, **16**, 1907042.
- 49 H. Zhang, W. Zhou, X. F. Lu, T. Chen and X. W. Lou, *Adv. Energy Mater.*, 2020, 2000882.
- 50 K. Yuan, D. Lützenkirchen-Hecht, L. Li, L. Shuai, Y. Li, R. Cao, M. Qiu, X. Zhuang, M. K. H. Leung, Y. Chen and U. Scherf, *J. Am. Chem. Soc.*, 2020, **142**, 2404–2412.
- 51 M. Zhang, Y. G. Wang, W. Chen, J. Dong, L. Zheng, J. Luo, J. Wan, S. Tian, W. C. Cheong, D. Wang and Y. Li, *J. Am. Chem. Soc.*, 2017, **139**, 10976–10979.
- 52 H. Shen, E. Gracia-Espino, J. Ma, K. Zang, J. Luo, L. Wang, S. Gao, X. Mamat, G. Hu, T. Wagberg and S. Guo, *Angew. Chem., Int. Ed.*, 2018, **56**, 13800–13804.
- 53 H. Zhang, P. An, W. Zhou, B. Y. Guan, P. Zhang, J. Dong and X. W. Lou, *Sci. Adv.*, 2018, **4**, eaao6657.
- 54 Y. Wang, J. Mao, X. Meng, L. Yu, D. Deng and X. Bao, *Chem. Rev.*, 2019, **119**, 1806–1854.
- 55 L. An, B. Huang, Y. Zhang, R. Wang, N. Zhang, T. Dai, P. Xi and C.-H. Yan, *Angew. Chem., Int. Ed.*, 2019, **58**, 9459–9463.
- 56 H. Shang, X. Zhou, J. Dong, A. Li, X. Zhao, Q. Liu, Y. Lin, J. Pei, Z. Li, Z. Jiang, D. Zhou, L. Zheng, Y. Wang, J. Zhou, Z. Yang, R. Cao, R. Sarangi, T. Sun, X. Yang, X. Zheng, W. Yan, Z. Zhuang, J. Li, W. Chen, D. Wang, J. Zhang and Y. Li, *Nat. Commun.*, 2020, **11**, 3049.
- 57 J. Zhang, Z. Zhao, Z. Xia and L. Dai, *Nat. Nanotechnol.*, 2015, **10**, 444–452.
- 58 S. Li, C. Cheng, X. Zhao, J. Schmidt and A. Thomas, *Angew. Chem., Int. Ed.*, 2018, **57**, 1856–1862.
- 59 X. Wei, D. Zheng, M. Zhao, H. Chen, X. Fan, B. Gao, L. Gu, Y. Guo, J. Qin, J. Wei, Y. Zhao and G. Zhang, *Angew. Chem., Int. Ed.*, 2020, **59**, 14639–14646.
- 60 Q. Li, W. Chen, H. Xiao, Y. Gong, Z. Li, L. Zheng, X. Zheng, W. Yan, W.-C. Cheong, R. Shen, N. Fu, L. Gu, Z. Zhuang, C. Chen, D. Wang, Q. Peng, J. Li and Y. Li, *Adv. Mater.*, 2018, **30**, 1800588.